Pergamon

Int. J. Heat Mass Transfer. Vol. 40, No. 13, pp. 3223–3235, 1997

Printed in Great Britain
0017–9310/97 $17.00+0.00

PII: S0017–9310(96)00321–3

Comparison of theory and experiments for reflection from microcontoured surfaces

DAVID W. COHN, KAKUEN TANG and RICHARD O. BUCKIUS†

Department of Mechanical and Industrial Engineering, University of Illinois, 1206 West Green Street, Urbana, IL 61801, U.S.A.

(*Received* 6 *June* 1996 *and in final form* 27 *August* 1996)

Abstract—Scattering from microcontoured surfaces, with length scales on the order of the wavelength of the incident radiant energy, requires consideration of electromagnetic scattering theory. A rigorous first-principle formulation to predict the bidirectional reflectivity for microcontoured or periodically profiled surfaces is presented. The focus of this investigation is on general scattering phenomena from such surfaces, on the specific experimental findings reported, and on previously reported experimental results that have not been predicted. Experimental data for the bidirectional reflectivity from nickel surfaces with sinusoidal and triangular profiles, and for chrome specimens with rectangular profiles, are presented. Comparisons between the reported experimental results and other measurements indicate very good agreement between the theoretical predictions and the experimental findings. © 1997 Elsevier Science Ltd.

1. INTRODUCTION

Surface scattering is of interest in many engineering disciplines, including manufacturing diagnostic systems used in the semiconductor industry [1, 2], rendering and visualization models in computer graphics [3], and thermal systems where radiation transport is important [4]. In such applications, general surface scattering from real surfaces with length scales on the order of the wavelength requires a complete consideration of the electromagnetic scattering theory. Simple and powerful approximations have been developed for various domains of surface roughness, yet rigorous analyses have recently become available for all degrees of roughness. This work presents a first-principle approach to predict thermal radiation properties for microcontoured surfaces and corresponding experimental results.

Radiation scattering studies include rigorous solutions, approximate methods and experimental predictions. Integral equation methods for electromagnetic theory, covering all ranges of the surface slope, height and wavelength, provide an exact approach to surface scattering analysis. These methods are based on the extinction theorem and Green's theorem, and there is no theoretical limitation on the roughness of the surface, nor on the dielectric properties of the surface. This general approach has been employed to predict the scattering phenomena of various surfaces: dielectric surfaces [4], perfectly conducting, randomly rough surfaces [5], non-Gaussian randomly rough surfaces [6], and very deep Gaussian randomly rough surfaces [7–12]. Recently, retro-reflection (energy reflected back into the incident solid angle region) for metallic and perfectly conducting random gratings was predicted with integral methods [13]. Such methods have been used to quantify back-scattering from a random rough dielectric surface [14] and a free-standing dielectric film or a dielectric film on a reflecting substrate [15]. The exact integral equations were developed for both one-dimensional perfectly conducting and dielectric surfaces with length scales on the order of the wavelength [16]. More recently, the extinction theorem boundary condition for integral formulations of radiation scattering from surfaces including multiply connected domains have been developed to study the reflection distribution from a perfectly conducting cylinder in front of a half-space [17].

Since the integral equation methods are very computationally intensive, a number of approximations have been used to predict scattering properties. Very common engineering approximations [18, 19] for the reflected energy from surfaces are to assume that the reflected energy occurs entirely in a single angle (specular reflection), over all angles (diffuse reflection), or in a combination of both specular and diffuse components [18–20]. Another approximate method is termed geometric optics, which limits the wavelength and roughness scales that can by quantified [21]. These models are only approximate and often require empirical approaches to determine specific results. Various electromagnetic theory approximations have also been used to predict the scattering from surfaces, including the Kirchhoff approximation which determines the field on the scatterer through the tangent plane approximation [22–24], and the perturbation approximation which expands the field into an asymptotic solution [25, 26]. While each approximate

† Author to whom correspondence should be addressed.

NOMENCLATURE

A solid angle response factor
A_ε, A_o, B_ε, B_o functions of G and its derivative
$\mathbf{E}$ electric field intensity vector
$E(x)$, $F(x)$, $H(x)$, $L(x)$ source functions; unknowns of the integral equations
F spectral response factor
G Green's function
$\mathbf{H}$ magnetic field intensity vector
k_o magnitude of wavevector of incident radiation
L_x, L_y extent of surface in x- and y-directions
m diffracted order, dimensionless
n, κ real and imaginary parts of refractive index
r_p, r_s scattering ratios defined in equations (17) and (18)
t time
V output signal
x, x', ξ horizontal coordinates
x_m, x_n points in the discrete domain of the surface profile function
z, z' vertical coordinates.

Greek symbols
α width of side wall
β space width
γ incident wave tapering parameter
ε, ε_o permittivity, permittivity of free space
$\hat{\varepsilon}$, ε_1, ε_2 complex dielectric constant, real part, imaginary part
$\varepsilon'_\lambda(\theta)$ directional spectral emissivity
$\zeta(x)$ surface profile function
θ_o angle of incidence
θ_s scattering or reflection angle
$\rho'_\lambda(\theta)$ directional–hemispherical spectral reflectivity
$\rho''_\lambda(\theta_o, \theta_s)$ bidirectional spectral reflection function
σ surface height [μm]; conductivity
τ repeat distance
Φ, Φ_s, Φ_o radiant power, scattered radiant power, incident radiant power
ω circular frequency of radiation
Ω solid angle.

Subscripts
x, y, z coordinates
ε complex dielectric constant
o incident
s scattered.

Superscripts
$>$ above the surface
ε complex dielectric constant.

approach is very useful within its own domain of validity [26–28], none are generally applicable for surfaces with length scales on the order of the wavelength.

Many experimental facilities have been set up to quantify reflection phenomena. An early experiment was developed to study the off-specular peaks phenomenon for both metals (nickel, copper and a nickel–copper alloy) and non-metals (magnesium-oxide ceramic) [21]. The basic parameters of surface roughness, wavelength and incident angle were systematically varied. Another experimental study [29] of surface roughness effects on reflection distribution considered aluminium alloy materials roughened by drawing them once across abrasive papers of various sizes and then coating them with an opaque layer of pure aluminium. Hesketh *et al.* [30–32] developed a system to study the spectral emittance of heavily doped-silicon profiled surfaces. The experimental results were compared to a geometric optics model. Ford *et al.* [33] developed a Fourier Transform Infrared (FTIR) spectrometer system to measure the bidirectional reflectivity for incident and reflected polar angles from 15° to 60°, mid-infrared wavelengths and different polarization states of the incident and reflected beams. Their experimental results on a randomly rough gold surface and a surface with triangular profile were in agreement with the corresponding theoretical predictions.

This work addresses the rigorous quantification of the bidirectional reflectivity and directional reflectivity for microcontoured surfaces, including surfaces with sinusoidal, triangular and rectangular one-dimensional grooved profiles. The primary goals are to present a rigorous approach to the prediction of thermal radiation properties, to compare predictions to new experimental results, and to analyze previously published experimental findings. The next section presents the analysis, including the directional radiation properties, governing equations and numerical formulation. The experimental system is then presented, and, finally, the theory predictions are compared to all the experimental studies.

2. ANALYSIS

The prediction of radiation properties requires three elements: the generation of the surface profile, the solution to the integral equations of scattering the prescribed surface, and the calculation of the thermal radiation properties. The governing equations require the solution to a set of integral equations for the electric and magnetic fields. This solution is developed

from the extinction theorem and Maxwell's equations. The calculation of the bidirectional reflectivity is then a direct integration of the integral equation solutions for each surface profile. The bidirectional reflectivity may be found for both metals and dielectrics. The regular or periodic surface profiles are generated as algebraic functions of the desired geometry.

2.1. *Directional radiation properties*

The bidirectional reflectivity is expressed as the ratio of π times the reflected radiant power per unit solid angle per unit area normal to the direction of reflection to the incident radiant power [18]. This is expressed in terms of the radiant power Φ and the solid angle Ω as

$$\rho''_\lambda(\theta_o, \theta_s) = \frac{\pi \dfrac{d\Phi_s}{d\Omega_s}}{\cos\theta_s \dfrac{d\Phi_o}{d\Omega_o}} \quad (1)$$

where the subscripts o and s denote the incident and scattered quantities, respectively. The directional–hemispherical reflectivity of the surface is obtained by integrating equation (1) over all the scattering angles, for a given incidence angle. The directional–hemispherical reflectivity is

$$\rho'_\lambda(\theta_o) = \frac{1}{\pi}\int_{2\pi} \rho''_\lambda(\theta_o, \theta_s)\cos\theta_s d\Omega_s. \quad (2)$$

Thus, computation of the bidirectional reflectivity requires the determination of the scattered power for the microcontoured surface. Integration of the bidirectional reflectivity over the scattered angles provides the directional reflectivity.

2.2. *Scattering formulation*

A brief overview of the analysis is provided here and a complete formulation of the governing equations for the surface scattering is presented elsewhere [14, 16]. The governing electromagnetic equations in Helmholtz form are derived from the Maxwell's equations [34] for one-dimensional surfaces with incidence and reflection in the same plane. The p-polarized field is given by

$$\mathbf{H}(x, z; t) = (0, H_y(x, z), 0)\exp(-i\omega t) \quad (3)$$

and

$$\mathbf{E}(x, z; t) = (E_x(x, z), 0, E_z(x, z))\exp(-i\omega t) \quad (4)$$

where $\mathbf{H}(x, z; t)$ is the magnetic field intensity vector, $\mathbf{E}(x, z; t)$ is the electric field intensity vector, ω is frequency and t is time. The components of each field are noted by the subscripts. The s-polarized field is given by

$$\mathbf{E}(x, z; t) = (0, E_y(x, z), 0)\exp(-i\omega t) \quad (5)$$

and

$$\mathbf{H}(x, z; t) = (H_x(x, z), 0, H_z(x, z))\exp(-i\omega t). \quad (6)$$

With Green's theorem and the jump boundary conditions, integral equations for the radiation scattering from surfaces are derived. The Green's function, G, for the two-dimensional Helmholtz equation, with a line source, is the Hankel function of the first kind and zeroth order. In the vacuum region above the surface $z > \zeta(x)$, the integral equations expressed in terms of the coordinate x for the p-polarized case are [14]

$$H(x) = H(x)_o + \int_{-\infty}^{\infty} [A_o(x; x')\, H(x') - B_o(x; x')\, L(x')]dx' \quad (7)$$

and for the material region below the surface, $z < \zeta(x)$,

$$H(x) = -\int_{-\infty}^{\infty} [A_\varepsilon(x; x')\, H(x') - \hat{\varepsilon} B_\varepsilon(x; x')\, L(x')]dx'. \quad (8)$$

The corresponding integral equations for the s-polarized field are

$$E(x) = E(x)_o + \int_{-\infty}^{\infty} [A_o(x; x')\, E(x') - B_o(x; x')\, F(x')]dx' \quad (9)$$

and

$$E(x) = -\int_{-\infty}^{\infty} [A_\varepsilon(x; x')\, E(x') - B_\varepsilon(x; x')\, F(x')]dx' \quad (10)$$

where $A_i(x; x')$ and $B_i(x; x')$ (i = o for perfectly conducting and $i = \varepsilon$ for general material properties) are functions of G and its derivative. In these equations, the limit as z goes to $\zeta(x)$ has been used to yield the following definitions [14]:

$$H(x)_o = H_y^{>}(x, \zeta(x))_o \quad (11)$$

$$E(x)_o = E_y^{>}(x, \zeta(x))_o \quad (12)$$

where $H(x)_o$ and $E(x)_o$ are the prescribed incident fields. $A_o(x; x')$ and $B_o(x; x')$ are obtained by setting $\hat{\varepsilon} = 1$ in $A_\varepsilon(x; x')$ and $B_\varepsilon(x; x')$, respectively. The unknowns in equations (7) and (8) are $H(x)$ and $L(x)$ for the p-polarized case, and in equations (9) and (10) they are $E(x)$ and $F(x)$ for the s-polarized case. $L(x)$ is related to derivative of $H(x)$ along the surface, and $F(x)$ is related to the derivative of $E(x)$ along the surface, as

$$L(x) = \left(-\zeta(x)\frac{\partial}{\partial x} + \frac{\partial}{\partial z}\right) H_y^{>}(x, \zeta(x)), \quad (13)$$

and

$$F(x) = \left(-\zeta(x)\frac{\partial}{\partial x} + \frac{\partial}{\partial z}\right) E_y^{>}(x, \zeta(x)). \quad (14)$$

With the incident power defined by the Poynting power theorem, the bidirectional reflection function of the p-polarized field is

$$\rho''_{\lambda p}(\theta_o, \theta_s) = \frac{1}{8} \frac{1}{L_x \cos\theta_s \cos\theta_o} |r_p(\theta_s)|^2 \quad (15)$$

and, similarly, for the s-polarized bidirectional refection function

$$\rho''_{\lambda s}(\theta_o, \theta_s) = \frac{1}{8} \frac{1}{L_x \cos\theta_s \cos\theta_o} |r_s(\theta_s)|^2 \quad (16)$$

where [14]

$$r_p(\theta_s) = \int_{-\infty}^{\infty} \exp\{-ik_o(x' \sin\theta_s + \zeta(x')\cos\theta_s)\} \cdot [ik_o(\zeta'(x')\sin\theta_s - \cos\theta_s)H(x') - L(x')]dx' \quad (17)$$

$$r_s(\theta_s) = \int_{-\infty}^{\infty} \exp\{-ik_o(x' \sin\theta_s + \zeta(x')\cos\theta_s)\} \cdot [ik_o(\zeta'(x')\sin\theta_s - \cos\theta_s)E(x') - F(x')]dx' \quad (18)$$

and L_x is the finite surface length. For unpolarized reflection, a simple average of equations (17) and (18) is taken. The unpolarized equations for bidirectional reflectivity are integrated over all θ_s to obtain unpolarized hemispherical reflectivity [equation (2)].

2.3. *Numerical implementation*

In order to solve the above equations, they are discretized. The first step is to convert the infinite range of integration to a finite domain. Abscissas are constructed at equally spaced points along the finite surface length, L_x. These equations were solved on a Cray Y-MP using LAPACK routines for the unknown $H(x_n)$, $L(x_n)$, $E(x_n)$ and $F(x_n)$. The solution procedure starts with the calculation of the matrix elements for a surface realization. They are stored in various quadrants of the matrix. For s-polarization, the matrix is immediately factored into its LU decomposition. In the p-polarized case, a quadrant must be multiplied by the $\hat{\varepsilon}$ factor and then factored. The incident field for each polarization at each surface element is then calculated. The incident field is either a plane wave or a Gaussian tapered wave. A tapered wave (with tapering parameters γ) attempts to eliminate surface edge effects [14]. The matrix equations are solved for their respective unknowns, $E(x_n)$ and $F(x_n)$ in the s-polarized case, and $H(x_n)$ and $L(x_n)$ in the p-polarized case.

The two factored matrices, for s- and p-polarizations, can be used for different incident angles and the same surface profile. On the Cray Y-MP, the LAPACK-b1 routines CGETRF and CGETRS are used to factor and solve, respectively, the matrix equations. Simple polynomial approximations [35] are used to obtain values for the Hankel functions required to evaluate the matrix elements.

The bidirectional reflectivity is an explicit integration over the L_x of $H(x)$ and $L(x)$, for the p-polarized case, and $E(x)$ and $F(x)$, for the s-polarized case. The bidirectional transmissivity is also an explicit integration over L_x of $H(x)$ and $L(x)$, for the p-polarized case, and $E(x)$ and $F(x)$, for the s-polarized case. The difference in the two integrations arises from the placement of the dielectric constant in the equations. The bidirectional reflectivity is a ratio of reflected energy to incident energy for every combination of incident angle and scattering angle.

The bidirectional reflectivity and the bidirectional transmissivity for a given polarization are the square of the magnitudes of the above equations relative to the incident energy. The bidirectional reflectivity is the average of the two polarizations. The bidirectional reflectivity and the bidirectional transmissivity are then integrated over all the reflection and transmission angles to determine the hemispherical values. For dielectric materials, these integrated functions must sum to one, which is used to verify conservation of energy. All the numerical results presented below conserve energy to within 1.0%.

3. FOURIER TRANSFORM INFRARED SPECTROMETER SYSTEM

3.1. *Experimental set up*

Bidirectional reflectivity measurements are performed with an FTIR system [33]. This system performs multiple wavelength measurements by utilizing a Michelson interferometer. The in-plane measurements are achieved by coupling the system with a variable-angle reflectometer. The system can provide results for reflection, transmission and emission of various interfaces, although only reflection measurements have been conducted.

An air-cooled Ever-Glo™ source operating at 1500 K is used in this experiment, and the detector is a high-sensitivity, liquid-nitrogen cooled mercury cadmium telluride (MCT), operating over the spectral range from 1 to 16 μm. The linear-response region of the MCT detector has been established, and all the measured data presented are within this region. Since the source beam is invisible, an HeNe laser for tracing the source beam's path through the optics is included in the facility. The laser beam also provides a reference for the wavelength.

The measurements were performed with the reflectometer system based on a modified Seagull™ variable-angle reflectivity accessory from Harrick Scientific Corporation. The accessory located in the sample compartment of the optical bench allows collection of in-plane bidirectional reflectivity data. Two ellipsoidal mirrors were installed above the horizontal sample focal plane. One mirror focuses the collimated energy beam that leaves the interferometer onto the sample while the other mirror collects the reflected energy to the detector element. Two plane mirrors guide the incident and reflected beams along the optical path. Those plane mirrors are free to rotate so that the

incident and reflected angles can be varied from 15° to 65°. Several limiting apertures at the inlet and exit ports of the reflectometer, combined with the source aperture of the spectrometer itself, provide control over the size of the incident and reflected solid angles for fertilizing the output energy level. For the experimental findings reported in Section 4.3, the solid angles of the incident and reflected energy are set in a planar angle of approximately 4°. Two polarizers are located in the inlet and exit ports of the reflectometer, providing the ability to polarize both the incident and reflected beams. They are aluminium wire grids on a KRS-5 substrate manufactured by Graesby Specac Inc.

3.2. *Data evaluation*

The bidirectional reflectivity can be calculated by using either the absolute or the relative method. In the absolute method, the intensities of the incident beam and reflected beam are measured, and the reflectivity can be calculated through dividing the reflected intensity by the incident flux and the cosine of the reflected angle and multiplying by π [see equation (1)]. The accuracy of this method is primarily dependent on the instrumentation error.

However, many instrumentation parameters can be canceled in the relative method. The outputs of the detector, $V_{\mathrm{ref}}(\lambda_c, \Delta\Omega_{o,c}, \Delta\Omega_{s,c})$, are recorded for a reference standard reflector in which the bidirectional reflectivity $\rho''_{\mathrm{ref}}(\lambda_c, \theta_o, \theta_s)$, is known as the calibration wavelength, λ_c, and various incident and reflected angles. The outputs of the sample of interest are measured, and the bidirectional reflectivity of the sample is calculated as follows:

$$\rho''_{\lambda}(\lambda, \theta_o, \theta_s) = \rho''_{\mathrm{ref}}(\lambda_c, \theta_o, \theta_s) \times \frac{V_m(\lambda, \Delta\Omega_o, \Delta\Omega_s)}{V_{\mathrm{ref}}(\lambda_c, \Delta\Omega_{o,c}, \Delta\Omega_{s,c})} F_{\lambda} A_{\Delta\Omega_o} A_{\Delta\Omega_s}. \quad (19)$$

In order to calculate the bidirectional reflectivity of the sample at the wavelengths other than λ_c, a spectral response factor, F_{λ}, is introduced in equation (19). The factor is determined by using an aluminium mirror which exhibits negligible reflectivity variation over the infrared region. In general, measurements of the reflection properties of the reference and the sample of interest using the same incident and reflected solid angles are preferred. However, in some situations, differences in the size of the incident and reflected solid angles between reflection measurements with the reference and the sample are inevitable. For a highly reflective reference material, a large solid angle provides a signal beyond the linear region of the MCT detector, while, for a dielectric sample, a small solid angle will result in a low signal-to-noise ratio. Since an intermediate value of the solid angle in which the outputs are within the linear region and provide a high signal-to-noise ratio does not always exist, incident and reflected solid angle factors, $A_{\Delta\Omega_o}$ and $A_{\Delta\Omega_s}$, are included in equation (19) to account for the difference in solid angles.

The reference standard reflector used in this experiment is Spectralon™ (sintered polytetrafluoroethylene), designed by Lapsphere, Inc. The material was selected because of its repeatable directional reflectance values with long-term stability and its diffuse reflectivity properties with an acceptable signal-to-noise ratio over the entire range of angles, wavelengths and polarization. The bidirectional reflectivity was measured by TMA Technologies, Inc. [36], using their CASI™ Scatterometer.

The overall system uncertainty for the reflection measurements is less than 10%. The estimation is based on the guidelines provided by Kim and Simon [37] as reported in ref. [33]. The major contributions of the experimental uncertainty include the quantification of the solid angles, wavelength and the reference TMA data.

4. RESULTS

4.1. *Surfaces*

The microcontoured surfaces considered include cases with previously reported experimental results and the surfaces experimentally investigated in this work. Experimental findings for surfaces made from doped silicon with rectangular profiles have been published by Hesketh *et al.* [30–32]. The uncertainty of their results is less than 5.0%. Additional experimental results for the bidirectional reflectivity for microconfigured metallic surfaces are obtained with the FTIR system and reported here. The geometry, radiative properties and associated results for the surfaces schematically shown in Fig. 1 are indicated in Table 1.

Geometrically, the three types of microconfigured surfaces considered include the following shapes: sinusoidal profiles, triangular profiles and rectangular profiles. These microconfigured surfaces are easily expressed in simple algebraic functions. Figure 1(a) shows a sinusoidal surface profile with the surface height, σ, and repeat distance, τ. The general triangular surface profile is shown in Fig. 1(b). The surface is described by three parameters. The surface peak parameter, f, is required in addition to the surface height, σ, and the repeat distance, τ. The peak parameter is between 0.0 and 1.0, with $f = 0.5$ yielding a symmetric triangular profile. The rectangular profile shown in Fig. 1(c) is described by the depth of the grooves, σ, the width of each groove, β (from the midpoints of the side walls), and the repeat distance between the midpoints of the grooves, τ. Figure 1(d) presents an SEM image of the chrome rectangular surface considered in this investigation.

The surfaces investigated by Hesketh *et al.* [30–32] provide relatively short repeat distances with two different groove depths. The corresponding ratios of surface height to repeat distance are relatively large, i.e. $\sigma/\tau = 0.07$ and 0.15, for these cases. The additional

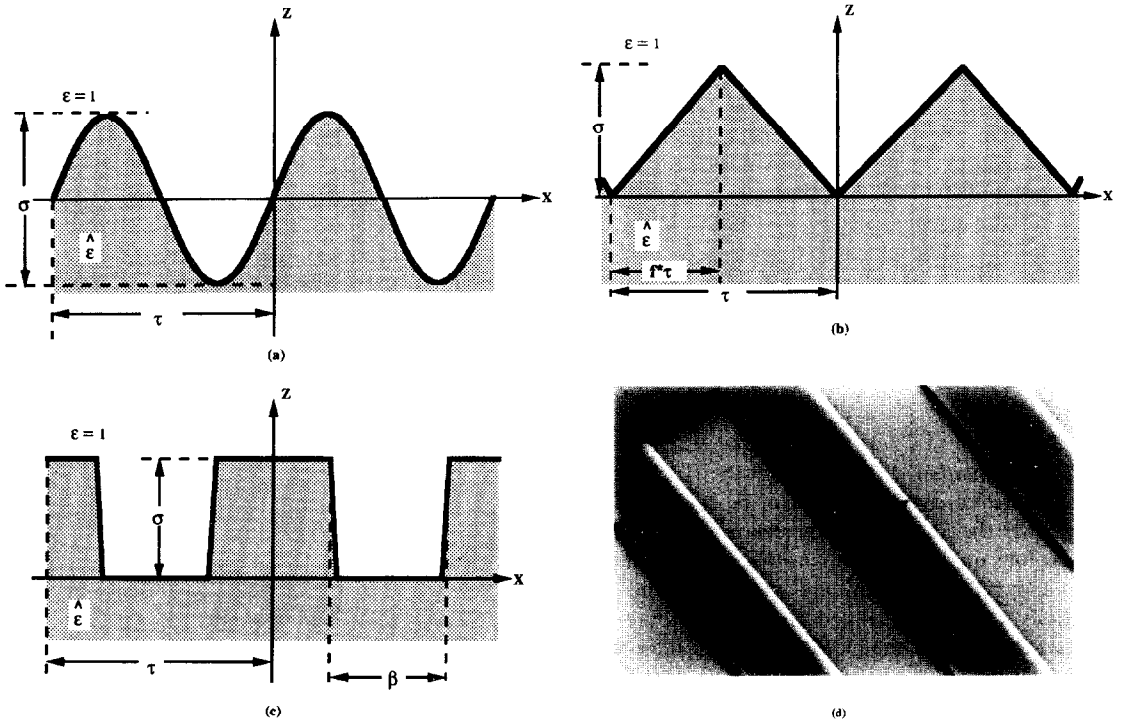

Fig. 1. Schematic of the surface cross section defining parameters for surfaces with sinusoidal profile (a), triangular profile (b), rectangular profile (c) and SEM of the chrome rectangular surface (d).

Table 1. Surface geometries and radiative properties

Profile	Geometric parameters (Fig. 1)			Material	Figure numbers
	τ [μm]	σ [μm]	Other		
Sinusoidal	35.6	1.12	None	Nickel–perfectly conducting	2 and 9
Triangular	16.7	1.38	$f = 0.5$	Nickel–perfectly conducting	3 and 10
Rectangular	20.0	0.94	$\beta = 10.0$ μm	Chrome–perfectly conducting	4 and 11
	10.0	0.70	$\beta = 6.30$ μm	Doped silicon	7
	10.0	1.50	$\beta = 7.30\mu$m	Doped silicon	5, 6 and 8

experimental results reported here include surfaces with sinusoidal and triangular profiles designed by Giddings & Lewis, Sheffield, Inc. [Fig. 1(d)], and a surface with a rectangular profile manufactured by VLSI Standards, Inc. The sinusoidal surface has a ratio of surface height to repeat distance of $\sigma/\tau = 0.031$, and the triangular and rectangular surfaces have larger values of σ/τ, 0.082 and 0.047, respectively.

The radiative properties of the rectangular grooves are those of doped silicon as reported by Hesketh *et al.* [30–32]. In order to predict and compare with the experimental results in these references, it was necessary to calculate the dielectric parameters n and κ, or equivalently ε_1 and ε_2, the real and imaginary parts of the complex dielectric constant. This was done by the method outlined by Hesketh *et al.* [30] using free carrier absorption theory. All parameters are given therein, except the high-frequency dielectric constant, which is provided in Hesketh [32]. The high-frequency dielectric constant has a value of 11.6. The optical properties for the metallic surfaces are approximated as perfectly conducting in the infrared region, i.e. n and κ are equal to infinity in the theoretical predictions. For the nickel and chrome surfaces in the wavelength region investigated, the perfectly conducting approximation provides an accurate prediction of surface reflection.

4.2. *Theoretical modal results*

The modal behavior of the bidirectional reflectivity indicates that, for a given incident angle, repeat distance and wavelength, energy is scattered only into certain angles. This behavior is illustrated in Figs. 2–

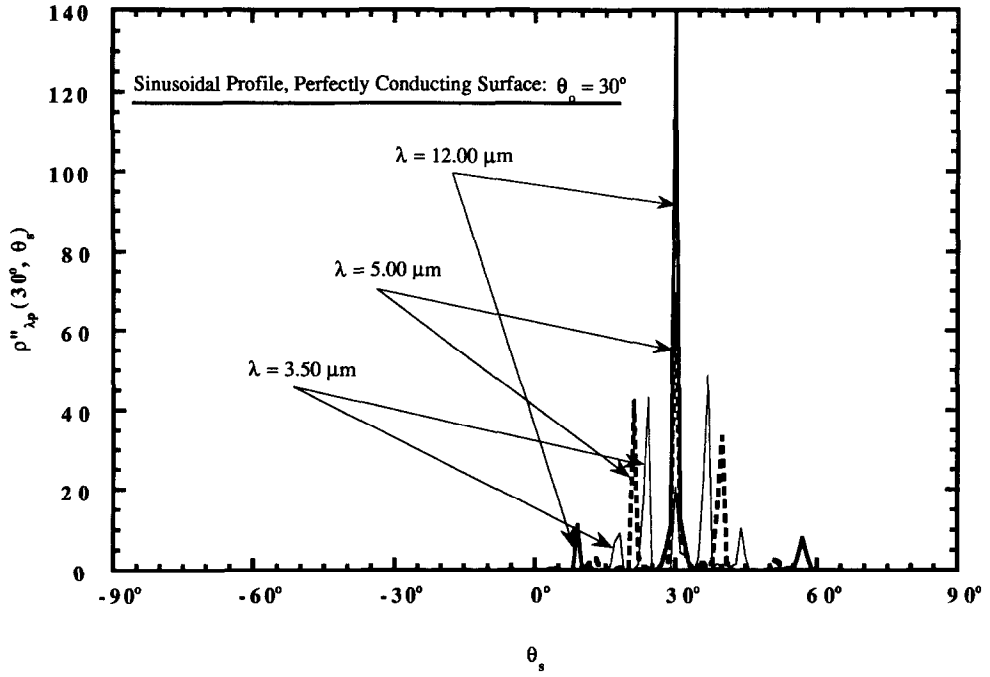

Fig. 2. P-polarized bidirectional reflectivity as a function of scattering angle and incident wavelength for a perfectly conducting surface with a sinusoidal profile ($\sigma = 1.12$ μm, $\tau = 35.60$ μm).

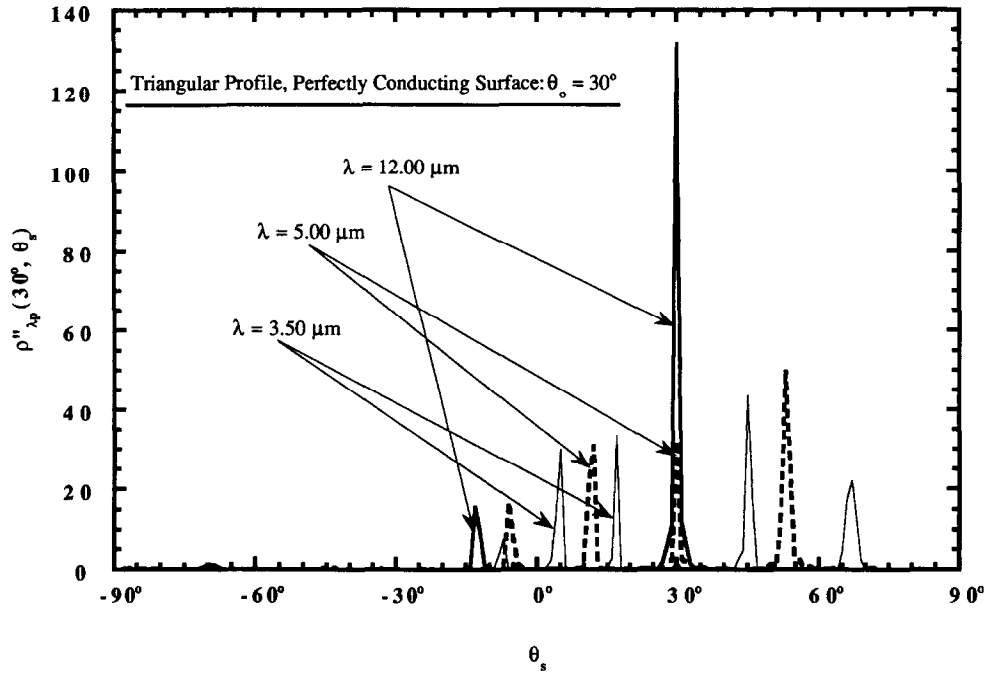

Fig. 3. P-polarized bidirectional reflectivity as a function of scattering angle and incident wavelength for a perfectly conducting surface with a triangular profile ($\sigma = 1.38$ μm, $\tau = 16.70$ μm).

4 for the perfectly conducting surfaces with sinusoidal, triangular and rectangular profiles. The location of the reflection modes is given by [38]

$$\sin\theta_s = \sin\theta_o + m\lambda/\tau\,;\, m = 0, \pm 1, \pm 2, \ldots \qquad (20)$$

where m is the diffracted order. As shown in Fig. 2, the bidirectional reflectivity for incident p-polarized radiation on the sinusoidal surface at an incident angle of 30° demonstrates this mode behavior. The bidirectional reflectivity for $\lambda = 3.50$ μm shows a concentration of peaks in a small region of the positive reflected angles, compared to the bidirectional reflectivity for $\lambda = 12.00$ μm, where the peaks are isolated. As wavelength increases, the ratio of λ/τ increases [see

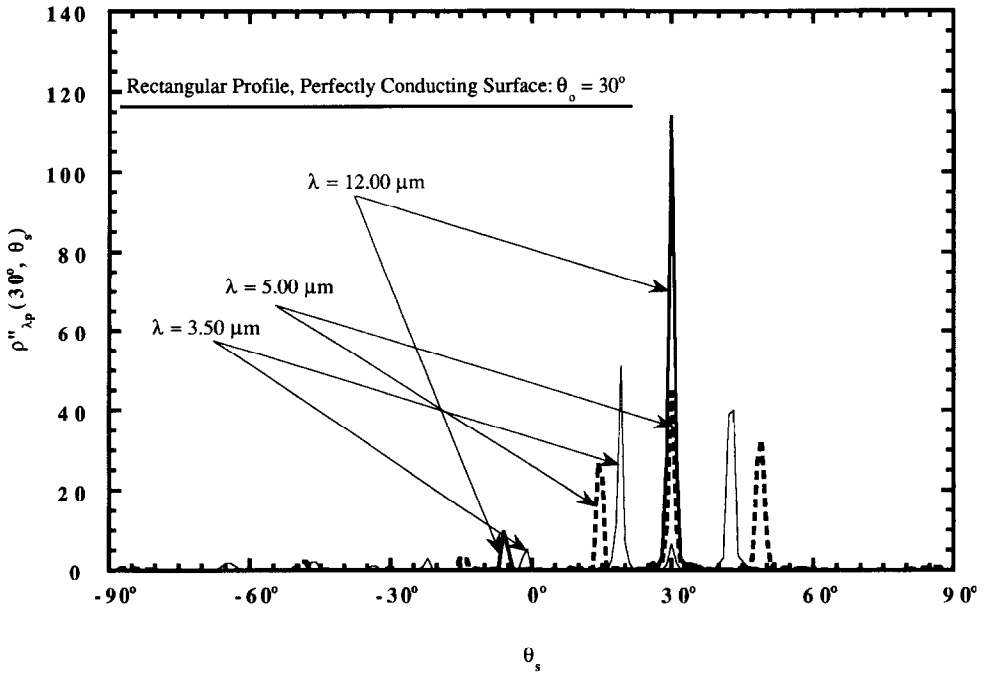

Fig. 4. P-polarized bidirectional reflectivity as a function of scattering angle and incident wavelength for a perfectly conducting surface with a rectangular profile ($\sigma = 0.94$ μm, $\tau = 20.00$ μm).

equation (20)], resulting in a greater angular distance between two consecutive peaks (e.g. θ_s for $m = 0$ and θ_s for $m = +1$).

Figures 3 and 4 present the bidirectional reflectivity for the same wavelengths and incident angle of incident p-polarized radiation on surfaces with triangular and rectangular profiles. Both rectangular and triangular profiles exhibit the modal behavior described above, and the angular region between two neighbouring reflection peaks decreases as wavelength decreases. Additionally, since the repeat distances of the triangular and rectangular profiles are approximately half that of the sinusoidal surface, the angular regions between two neighbouring reflection peaks are much wider, and the surfaces exhibit retro-reflection phenomena.

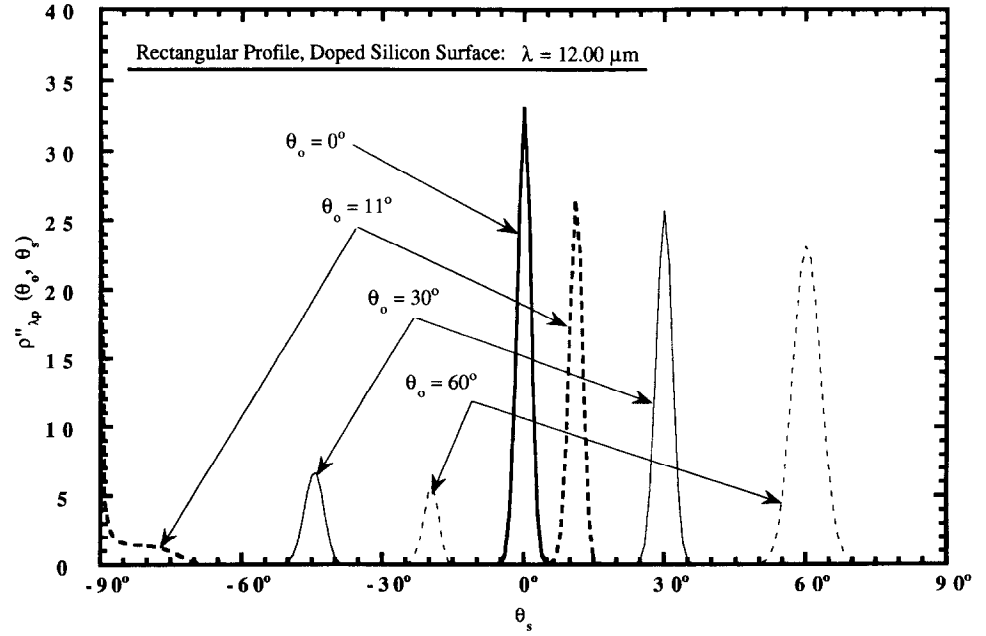

Fig. 5. P-polarized bidirectional reflectivity as a function of scattering angle and incident angle for a doped silicon surface with a rectangular profile ($\tau = 10.00$ μm, $\sigma = 1.50$ μm, $\beta = 7.30$ μm, $\gamma = 4.0$, $\lambda = 12.0$ μm).

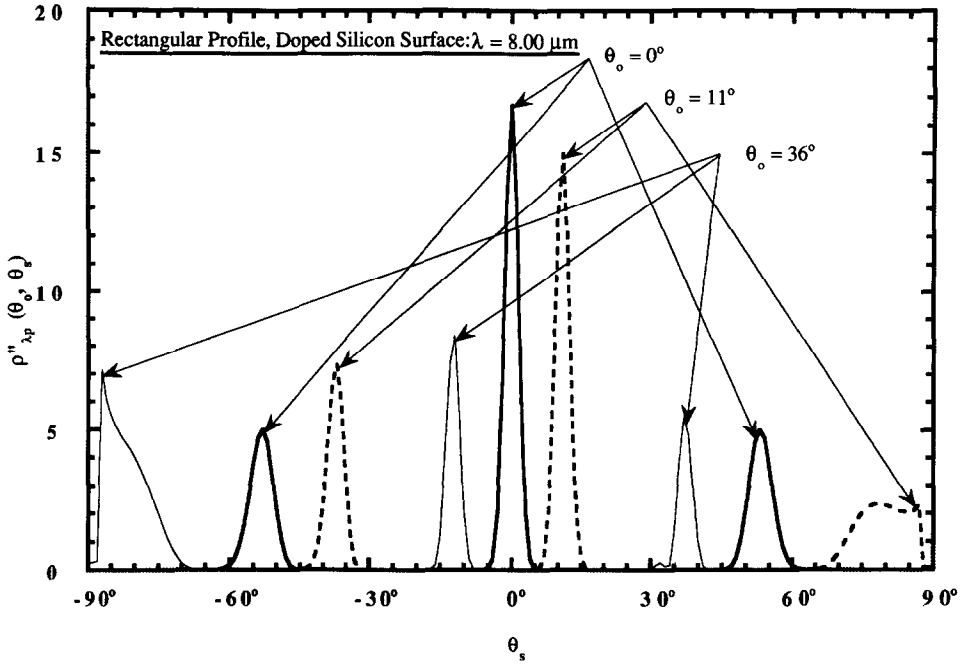

Fig. 6. P-polarized bidirectional reflectivity as a function of scattering angle and incident angle for a doped silicon surface with a rectangular profile ($\tau = 10.00$ μm, $\sigma = 1.50$ μm, $\beta = 7.30$ μm, $\gamma = 4.0$, $\lambda = 8.0$ μm).

In addition to wavelength, incident angle also has important effects on scattering phenomena. The bidirectional reflectivity for incident p-polarized radiation at various incident angles of surfaces with rectangular profiles demonstrates the modal behavior in Figs. 5 and 6. When one of these modes is at $\theta_s = \pm 90°$, then energy in that mode does not leave the surface. Thus there is less total reflection (reflection reduction) at incident angles that yield modes at $\theta_s = \pm 90°$, and the mode enhances the corresponding absorptivity of the surface. In the present case, this reflection reduction can only occur if resonant modes are set up in the cavities made by the grooves which then direct energy away from the surface. This surface wave is indicated in Fig. 5 at the scattering angle $\theta_s = -90°$ for $\theta_o = 11°$. The profiled surface specified in Fig. 6 exhibits such reflection reduction near $\theta_o = 11°$ and 36°.

Surface material also plays an important role on scattering phenomena. Although the rectangular profiles presented in Figs. 4–6 are the same order of magnitude in surface geometric parameters (τ, β and σ), the magnitude of the bidirectional reflectivity in Fig. 4 is much larger than in Figs. 5 and 6. For perfectly conducting surfaces, all the incident energy is reflected, while, for the doped silicon surfaces, a fraction of the incident energy will be absorbed. Thus, the magnitudes of the bidirectional reflectivity for the perfectly conducting surfaces (Fig. 4) is much larger than for the doped silicon surfaces (Figs. 5 and 6).

4.3. *Experimental and theoretical comparisons*

Directional–hemispherical reflectivity is obtained directly from the bidirectional reflectivity, similar to those in Figs. 5 and 6, as indicated in equation (2). For the doped silicon surfaces, the directional–hemispherical spectral reflectivity predictions of p-polarized incident radiation are shown in Fig. 7 along with the experimental data of Hesketh [32]. Since the directional spectral emissivity is presented in ref. [32], the experimental directional spectral reflectivity is calculated from Kirchhoff's law and conservation of energy,

$$\rho'_\lambda(\theta) = 1 - \varepsilon'_\lambda(\theta). \tag{21}$$

The numerical predictions and experimental results show the same trends. Moreover, the predicted results show the same reflection reductions in the same angles as the experimental results. The location of the reflected angles where reduction occur is given by Hesketh *et al.* [30] as

$$\sin\theta = \frac{\varepsilon_1(\lambda)}{1+\varepsilon_1(\lambda)} - \frac{m\lambda}{\tau} \tag{22}$$

where ε_1 is the real part of the complex dielectric constant, and m is the diffracted order. Hesketh *et al.* [30] state that these reductions in the p-polarized reflection can be attributed to the "launching of a surface electromagnetic wave," that is, a wave that travels along the surface. S-polarized results are very smooth and are not presented. Also, directional spectral reflectivity does not change significantly for wavelengths larger than the repeat distance.

The p-polarized reflection results for the surfaces with rectangular profiles and $\sigma = 1.50$ μm are shown with experimental values in Fig. 8. Good agreement between the numerical and experimental results were

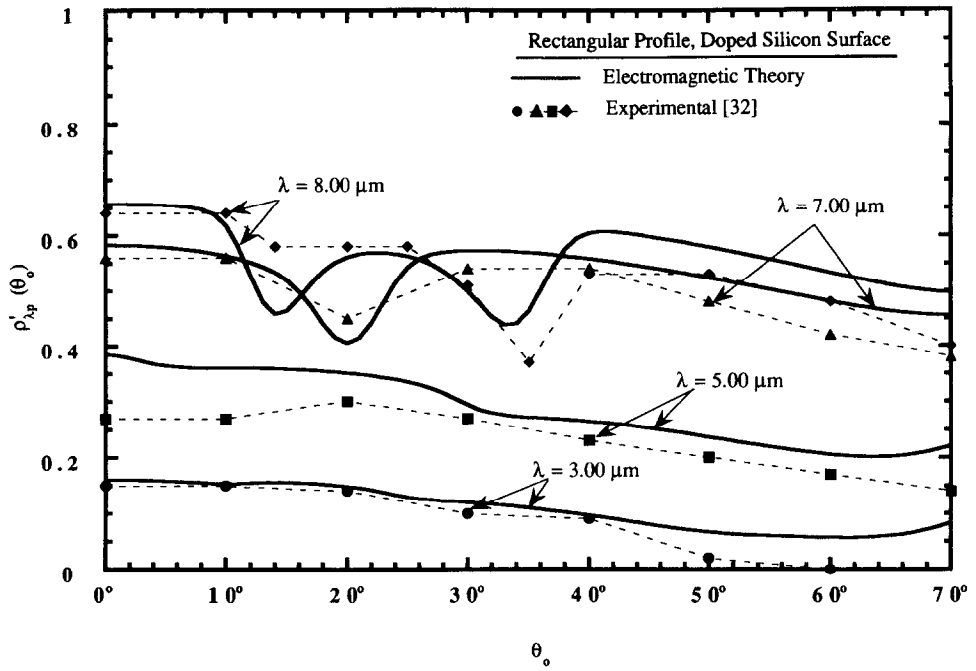

Fig. 7. P-polarized directional reflectivity as a function of scattering angle and incident angle for a doped silicon surface with a rectangular profile ($\tau = 10.00\ \mu m$, $\sigma = 0.70\ \mu m$, $\beta = 6.30\ \mu m$, $\gamma = 4.0$) [32].

obtained at most wavelengths, yet the predicted reflection reductions are much greater than the experimental values. The profiles specified in Fig. 8 exhibit reductions at 11° and 21° at wavelengths of 12.00 and 14.00 μm. To understand the difference between the predictions and the experiments, a variation in surface repeat distance was investigated. For surfaces whose periodicity is perfect, the magnitude of the predicted reflection reductions are strong as shown in Fig. 8 for $\lambda = 12.00$ and 14.00 μm. To assess the effect of experimental construction precision on the minimums in the p-polarized reflection results, special surfaces were numerically constructed. Rectangular profiles were constructed with the groove dimensions altered

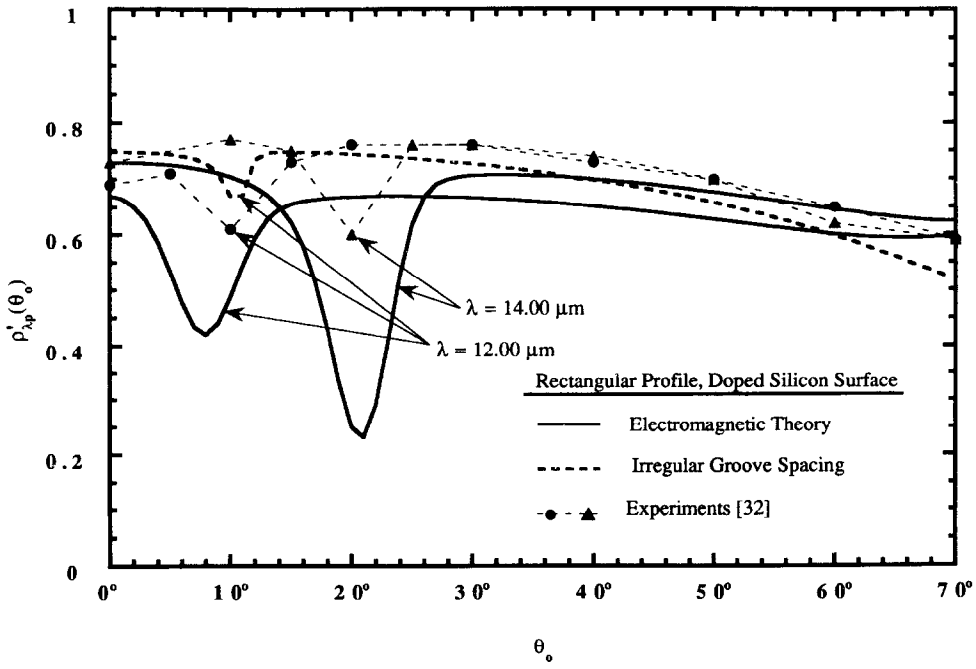

Fig. 8. P-polarized directional reflectivity as a function of scattering angle and incident angle for a doped silicon surface with a rectangular profile ($\tau = 10.00\ \mu m$, $\sigma = 1.50\ \mu m$, $\beta = 7.30\ \mu m$, $\gamma = 4.0$) [32].

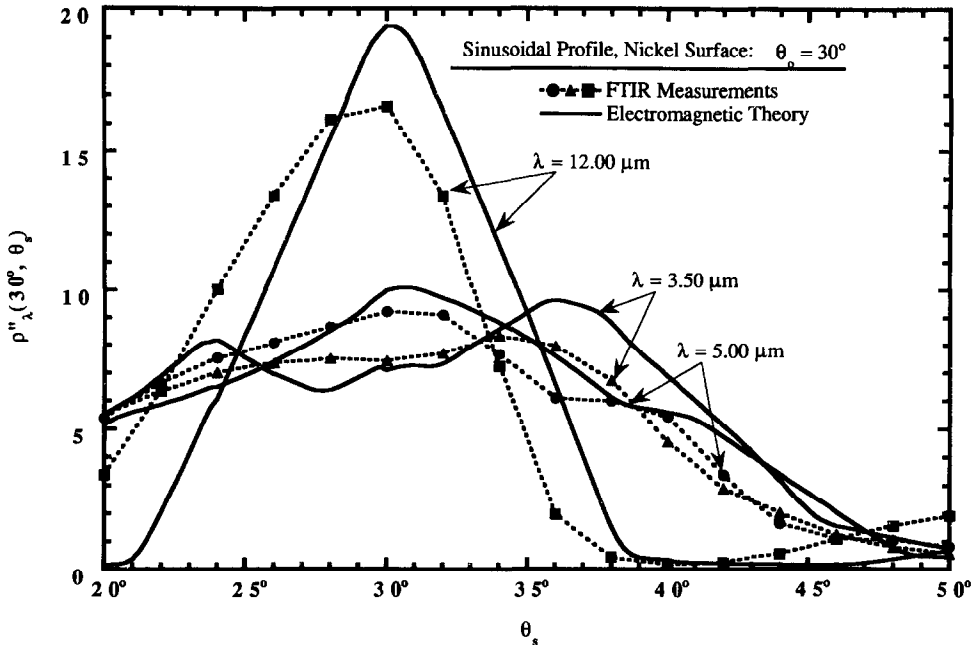

Fig. 9. Comparison between electromagnetic theory and experimental results as a function of scattering angle and incident wavelength for a nickel surface with a sinusoidal profile.

so that the distance between corresponding points on each groove was not exactly τ, but varied from that value by approximately 10%. The results for surfaces with such irregular groove spacing are shown in Fig. 8 and they indicate that the reductions are sharply attenuated. Since Hesketh [32] states that the width measurements have a variation of 10% and the depth variations of 20%, these construction difficulties have apparently degraded the reduction effects numerically predicted for these gratings.

Figures 9–11 present the predictions and FTIR experimental results for the surfaces with sinusoidal, triangular and rectangular profiles. The results of the electromagnetic theory presented in Figs. 9–11 have been integrated over the experimentally measured solid angle of $\pm 4^\circ$ about incident and reflected angles.

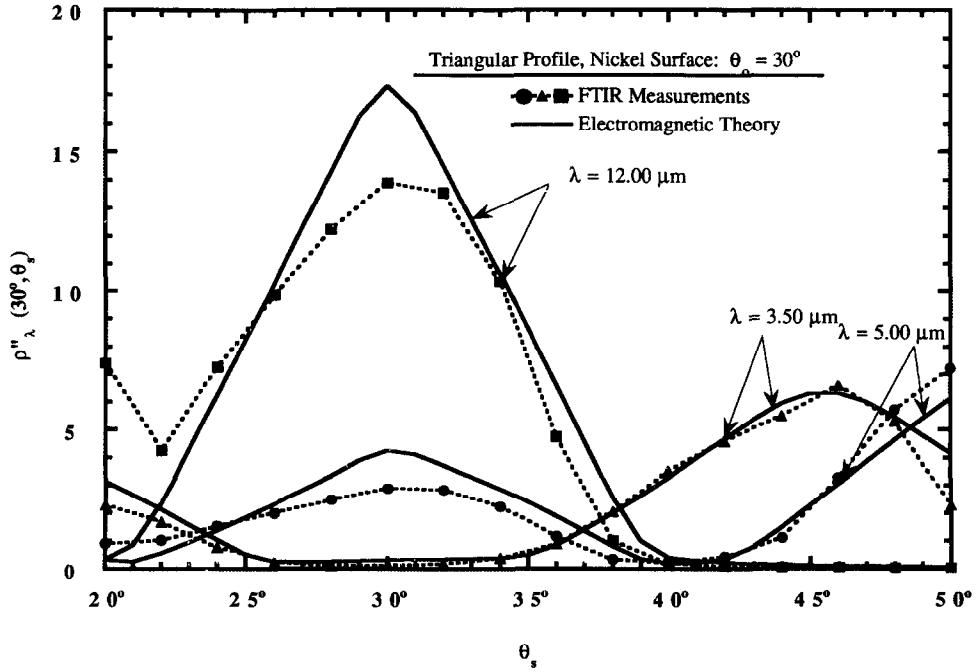

Fig. 10. Comparison between electromagnetic theory and experimental results as a function of scattering angle and incident wavelength for a nickel surface with a triangular profile.

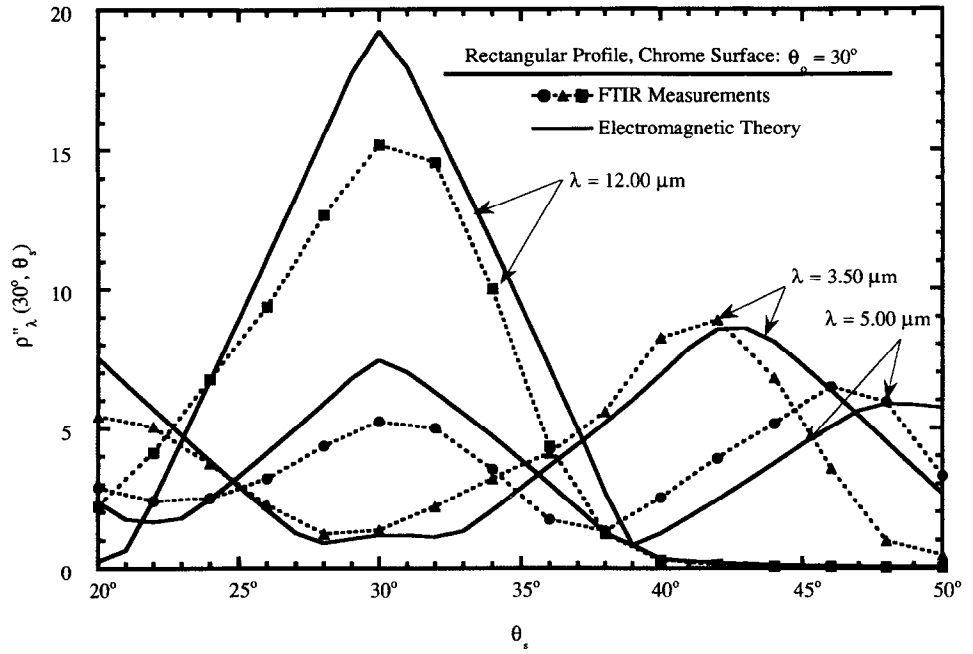

Fig. 11. Comparison between electromagnetic theory and experimental results as a function of scattering angle and incident wavelength for a chrome surface with a rectangular profile.

In general, the experimental results are very similar to the electromagnetic theory predictions in both trend and absolute magnitude. The bidirectional reflectivity for the sinusoidal surface at an incident angle of 30° for wavelengths of 3.50, 5.00 and 12.00 μm is presented in Fig. 9. For $\lambda = 12.00$ μm, which is on the order of the repeat distance, the sample exhibits specular reflection with a single isolated reflection peak in the scattering angles investigated as previously discussed (Fig. 2). Large values of reflection are predicted about the scattering angles, $\theta_s = 30°$. For $\lambda = 5.00$ μm, the reflection distribution spans a wider range of the scattering angle than that of $\lambda = 12.00$ μm. The bidirectional reflectivity is even more diffuse for $\lambda = 3.50$ μm. Comparing the modal predictions in Fig. 2 and the experimental findings for $\lambda = 5.00$ and 12.00 μm, the fine detail of the modal predictions are reduced by the finite solid angles of the experiments. However, the modes are observed at $\theta_s = 30°$ for $\lambda = 5.00$ μm, and $\theta_s = 24°$ and 37° for $\lambda = 3.50$ μm.

The results for the surfaces with a triangular profile (Fig. 10) and rectangular profile (Fig. 11) indicate a reflection distribution that is relatively specular and similar to that of the sinusoidal surface for $\lambda = 12.00$ μm. However, for $\lambda = 5.00$ μm, the reflection distribution of the triangular and rectangular profiled surfaces exhibit the modal structure shown in Figs. 3 and 4, respectively. For $\lambda = 3.50$ μm, a similar phenomenon is observed. Since the modal reflection predictions in Figs. 3 and 4 indicate a wider distribution of peaks in scattering angle, the integration of the bidirectional reflectivity over the experimental solid angle of $\pm 4°$ does not eliminate the modes. The peaks in both the experimental results and the integrated predictions are relatively distinct. Thus, the comparisons of the magnitude of the predicted and experimental results are quite good, and the reflection phenomenon is strongly dependent upon the repeat distance, τ, and surface slope, σ/τ. Similar dependencies have been observed in random rough surfaces [27, 28, 39].

5. CONCLUSIONS

The rigorous electromagnetic theory approach provides a means of predicting the scattering behavior of microconfigured surfaces. It is, in principle, an exact method since no fundamental theoretical approximations are made in its formulation. This research has focused on general scattering phenomena and on specific cases where experimental observations are available. In particular, the spectral directional reflectivity for silicon surfaces with rectangular profiles, experimental results form previous studies are in good agreement with the present theoretical predictions at various incident angles. The FTIR measurements of bidirectional reflectivity for metallic surface with sinusoidal, triangular and rectangular profiles agree well with the corresponding theoretical predictions in both trend and magnitude. In general, for the various geometries, length scales, and material properties investigated, the agreement of the predictions with experimental data is very good.

Acknowledgements—The comments provided on this paper by Ralph A. Dimenna are gratefully acknowledged. Support for the work has been provided by the National Science Foundation (NSF CTS 95-31772), the University of Illinois

Research Board, Richard W. Kritzer Endowment Fund, Pittsburgh Supercomputing Center and the National Center for Supercomputing Applications.

REFERENCES

1. Chinnock, C., Laser-based systems easily find semiconductor defects. *Laser Focus World*, 1994, November, 59–66.
2. Howland, R. S. and Larson, C. T., How to correlate laser-scattering surface inspection. *Laser Focus World*, 1995, July, 99–103.
3. Sillion, F. X., Arvo, J. A., Westin, S. H. and Greenberg, D. P., A global illumination solution for general reflectance distributions. *Computer Graphics*, 1991, **25,** 187–196.
4. Drolen, B. L., Bidirectional reflectance and specularity of twelve spacecraft thermal control materials. *Journal of Thermophysics and Heat Transfer*, 1992, **6,** 672–679.
5. Maystre, D., Sur la diffraction d'une onde plane electromagnetique par un reseau metallique. *Optical Communications*, 1973, **8,** 216–219.
6. Axline, R. M. and Fung, A. K., Numerical computation of scattering from a perfectly conducting random surface. *IEEE Transactions in Antennas and Propagation*, 1988, **AP-26,** 482–488.
7. Wu, S. C., Chen, F. M. and Fung, A. K., Scattering from non-Gaussian randomly rough surfaces—cylindrical case. *IEEE Transactions in Geoscience Remote Sensing*, 1988, **26,** 790–798.
8. Nieto-Vesperinas, M. and Soto-Crespo, J. M., Light-diffracted intensities from very deep gratings. *Physics Review B*, 1988, **38,** 7250–7259.
9. Nieto-Vesperinas, M. and Sánchez-Gil, J. A., Light transmission from a randomly rough dielectric diffuser: theoretical and experimental results. *Optical Letters*, 1990, **15,** 1261–1263.
10. Nieto-Vesperinas, M. and Sánchez-Gil, J. A., Light scattering from a random rough interface with total internal reflection. *Journal of the Optical Society of America A*, 1992, **9,** 424–436.
11. Sánchez-Gil, J. A. and Nieto-Vesperinas, M., Light scattering from random dielectric surfaces. *Journal of the Optical Society of America A*, 1991, **8,** 1270–1286.
12. Soto-Crespo, J. M. and Nieto-Vesperinas, M., Electromagnetic scattering from very rough random surfaces and deep reflection gratings. *Journal of the Optical Society of America A*, 1989, **6,** 367–384.
13. Maradudin, A. A., Méndez, E. R. and Michel, T., Backscattering effects in the elastic scattering of p-polarized light from a large-amplitude random metallic grating, *Optical Letters*, 1989, **14,** 151–153.
14. Maradudin, A. A., Michel, T., McGurn, A. R. and Méndez, E. R., Enhanced backscattering of light from a random grating. *Annals of Physics*, 1990, **203,** 255–307.
15. Maradudin, A. A., Lu, J. Q., Michel, T., Gu, T. H., Dainty, J. C., Sant, A. J., Méndez, E. R. and Nieto-Vesperinas, M., Enhanced backscattering and transmission of light from random surfaces on semi-infinite substrates and thin films. *Waves in Random Media*, 1991, **3,** S129–S141.
16. Dimenna, R. A. and Buckius, R. O., Electromagnetic theory predictions of the directional scattering from triangular surfaces. *ASME Journal of Heat Transfer*, 1994, **116,** 639–645.
17. Madrazo, A. and Nieto-Vesperinas, M., Scattering of electromagnetic waves from a cylinder in front of a conducting plane. *Journal of the Optical Society of America A*, 1995, **12,** 1298–1309.
18. Brewster, M. Q., *Thermal Radiative Transfer & Properties*, 1st edn. John Wiley, New York, 1992.
19. Siegel, R. and Howell, J. R., *Thermal Radiation Heat Transfer*. Hemisphere, New York, 1992.
20. Hesketh, P. J., Gebhart, B. and Zemel, J. N., Measurements of the spectral and directional emission from microgrooved silicon surfaces. *ASME Journal of Heat Transfer*, 1988, **110,** 680–686.
21. Torrance, K. E. and Sparrow, E. A., Theory of off-specular reflection from roughened surfaces. *Journal of the Optical Society of America*, 1967, **57,** 1105–1114.
22. Davies, H., The reflection of electromagnetic waves from a rough surface. *Proceedings of the IEEE*, Vol. 101, Part IV, pp. 209–214, 1954.
23. Beckmann, P. and Spizzichino, A., *The Scattering of Electromagnetic Waves from Rough Surfaces*. Macmillan, New York, 1963.
24. Faure-Geors, H. and Maystre, D., Improvement of the Kirchhoff approximation for scattering from rough surface. *Journal of the Optical Society of America A*, 1989, **6,** 532–542.
25. Ogilvy, J. A., Wave scattering from rough surfaces. *Reports on the Progress of Physics*, 1987, **50,** 1553–1608.
26. Thorsos, E. I. and Jackson, D. R., The validity of the perturbation approximation for rough surface scattering using a Gaussian roughness spectrum. *Journal of the Acoustical Society of America*, 1989, **86,** 261–277.
27. Dimenna, R. A. and Buckius, R. O., Quantifying specular approximations for angular scattering from perfectly conducting random rough surfaces. *Journal of Thermophysics and Heat Transfer*, 1994, **8,** 393–399.
28. Tang, K., Dimenna, R. A. and Buckius, R. O., Regions of validity of the geometric optics approximation for angular scattering from very rough surfaces. *International Journal of Heat and Mass Transfer*, 1997, **40,** 45–59.
29. Smith, T. F., Suiter, R. L. and Kanayama, K., Bidirectional reflectance measurements for one-dimensional, randomly rough surfaces. In *Progress in Astronautics and Aeronautics: Heat Transfer, Thermal Control and Heat Pipes*, Olstead, W. ed. AIAA, New York, 1979, pp. 189–208.
30. Hesketh, J. P., Gebhart, B. and Zemel, J. N., Polarized spectral emittance from periodic micromachined surfaces, I. Doped silicon: the normal direction. *Physics Review B*, 1988, **37,** 10795–10802.
31. Hesketh, P. J., Gebhart, B. and Zemel, J. N., Polarized spectral emittance from periodic micromachined surfaces. II. Doped silicon: angular variation. *Physics Reviews B*, 1988, **37,** 10803–10813.
32. Hesketh, P. J., The emittance of heavily doped microconfigured silicon surfaces. Ph.D. thesis, University of Pennsylvania., Philadelphia, PA, 1987.
33. Ford, J. N., Tang, K. and Buckius, R. O., Fourier transform infrared system measurement of the bi-directional reflectivity of diffuse and grooved surfaces. *ASME Journal of Heat Transfer*, 1995, **117,** 955–962.
34. Stratton, J. A., *Electromagnetic Theory*, 1st edn. McGraw-Hill, New York, 1941, pp. 23–131.
35. Abramowitz, M. and Stegun, I. A., eds, *Handbook of Mathematical Functions*, 9th edn., Dover, New York, 1965.
36. TMA, Inc., Bidirectional reflectivity data for Spectralon™ and Infragold™ samples. Bozeman, MT, 1994.
37. Kim, J. H. and Simon, T. W., Journal of heat transfer policy on reporting uncertainties in experimental measurements and results, *ASME Journal of Heat Transfer*, 1993, **115,** 5–6.
38. Klein, M. V. and Furtak, T. E., *Optics*. John Wiley, New York, 1986, pp. 253–328.
39. Yang, Y. and Buckius, R. O., Surface length scale contributions to the directional and hemispherical emissivity and reflectivity. *Journal of Thermophysics and Heat Transfer*, 1995, **9,** 653–659.